https://doi.org/10.5194/egusphere-2026-1160
Preprint. Discussion started: 20 May 2026

Two decades of GNSS-IR observations reveal an asymmetric decline in coastal sea ice phenology of the Beaufort Sea

Minfeng Song[1], Xiaolei Wang[1,*], Zhenyu He[2], Dongzhen Jia[1], Ruya Xiao[1], Xiufeng He[1]

[1]School of Earth Sciences and Engineering, Hohai University, Nanjing, Jiangsu 211100, China
[2]College of Information Science and Engineering, Hohai University, Changzhou, Jiangsu 213200, China

Correspondence to: Xiaolei Wang (chd_wxl@qq.com)

Abstract. Arctic coastal sea ice phenology is a critical climate indicator, yet sub-kilometer long-term observations remain scarce, limiting our understanding of complex local freeze-thaw dynamics. This study investigates the long-term evolution and thermodynamic drivers of coastal sea ice using a continuous, 20-year (2003–2023) high-resolution dataset derived from ground-based GNSS Interferometric Reflectometry (GNSS-IR) at Tuktoyaktuk in the Beaufort Sea. By employing a physics-based Amplitude Integration Factor (AIF) method, we successfully bridged decadal hardware discrepancies to extract an uninterrupted, thermodynamically consistent climatological record. Trend analysis of the 20-year record reveals a statistically significant shortening of the continuous ice season by 4.63 days per decade ($p = 0.04$). This climatological decline is profoundly asymmetric, driven primarily by a substantially delayed autumn freeze-up (+3.40 days per decade) rather than an advanced spring breakup (-1.42 days per decade), underscoring the dominant influence of enhanced summer oceanic heat uptake and thermal memory. The physical reliability of these localized observations is corroborated by their strong coupling with accumulated Freezing Degree-Days ($R^2 = 0.74$). Crucially, cross-scale comparisons demonstrate that GNSS-IR detects autumn freeze-up onset 5.5 ± 3.7 days earlier than 4-km gridded satellite products (IMS). This systemic lead time confirms the unique capability of GNSS-IR to resolve initial nearshore frazil ice formation—a critical sub-grid thermodynamic process typically diluted in coarse-resolution remote sensing. Ultimately, this work provides an essential high-resolution baseline for validating regional climate models.

1 Introduction

The Arctic cryosphere serves as a highly sensitive sentinel for global climate change. Driven by a phenomenon known as Arctic Amplification, the region has warmed at a rate nearly three to four times the global average over the past four decades(Previdi et al., 2021; Serreze and Barry, 2011). This amplified warming is not merely a surface temperature anomaly but involves complex feedback loops between the atmosphere, ocean, and sea ice. The most visible manifestation of this change is the dramatic decline in Arctic sea ice extent, thickness, and age(Comiso et al., 2008; Kwok, 2018). According to the *2024 NOAA Arctic Report Card* (Meier et al., 2024), the Arctic sea ice extent in September 2024 was the sixth lowest in the 46-year satellite record, reinforcing a trend where the last 18 years (2007–2024) correspond to the 18 lowest minima ever

https://doi.org/10.5194/egusphere-2026-1160
Preprint. Discussion started: 20 May 2026

observed (Meier et al., 2024). While the reduction in spatial extent is well-documented, the shift in sea ice phenology—defined as the seasonal timing of melt onset, breakup, freeze-up, and the duration of the open-water season—represents a more dynamic and ecologically critical dimension of change. Satellite records indicate that the melt season has lengthened by 5–10 days per decade across much of the Arctic Ocean (Markus et al., 2009; Stroeve et al., 2014), a shift that fundamentally alters the regional surface energy budget.

These phenological shifts are particularly acute in the Arctic Coastal Zones (ACZs), the narrow interface where terrestrial permafrost, landfast sea ice, and the open ocean interact. In these shallow nearshore waters, the lengthening of the open-water season triggers a potent ice-albedo feedback mechanism. Earlier spring breakup exposes the low-albedo ocean surface to peak summer solar radiation, leading to a substantial increase in oceanic heat uptake—estimated at an additional 8–15 MJ m^{-2} per season in the Beaufort Sea (Perovich et al., 2007). This accumulated heat delays the formation of sea ice in autumn, creating a "thermal memory" effect that further warms the lower atmosphere (Cox et al., 2017). The consequences of these changes extend far beyond thermodynamics. For Arctic coastal communities, landfast ice (fast ice) serves as a vital extension of the land, supporting subsistence hunting, transportation corridors, and cultural activities (Eicken et al., 2009). Moreover, the delayed freeze-up leaves the coastline exposed to autumn storm surges for longer periods. When combined with thermal abrasion from warmer waters, this has accelerated coastal permafrost erosion rates to over 10 meters per year at vulnerable sites along the Yukon and Northwest Territories coastlines (Lantuit et al., 2012; Overeem et al., 2011).

Despite the urgent scientific and societal need to monitor these coastal dynamics, a critical observational gap persists at the local coastal scale (< 10 km). Quantifying phenological trends with the precision required for climate attribution, infrastructure planning, and model validation remains a formidable challenge due to the inherent limitations of current observing systems in the complex coastal boundary zone.

Satellite remote sensing faces severe constraints when applied to nearshore environments. Passive microwave sensors provide invaluable daily pan-Arctic records, yet their coarse spatial resolutions (12.5–25 km) inevitably suffer from 'land spillover' contamination nearshore (Cavalieri et al., 1999; Meier et al., 2017). Conversely, high-resolution Synthetic Aperture Radar (SAR) is constrained by low temporal repeat cycles (Antonova et al., 2016) and interpretative ambiguities during the melt season (Dierking, 2013; Yackel and Barber, 2000). Optical sensors are frequently rendered unusable by persistent Arctic cloud cover and polar night (Li et al., 2023).. Meanwhile, in-situ observations provide crucial ground truth but suffer from extreme spatial sparsity and high logistical costs in dynamic, ice-infested waters (Pierson et al., 2011). Consequently, systematic, sub-kilometer decadal records remain virtually absent , limiting our ability to validate high-resolution climate models (Post et al., 2019).

To bridge this resolution and continuity gap, Global Navigation Satellite System Interferometric Reflectometry (GNSS-IR) has emerged as a disruptive, cost-effective remote sensing technique. GNSS-IR exploits the interference pattern formed by the superposition of the direct signal from a navigation satellite (GPS, GLONASS, Galileo, BeiDou) and the signal reflected from the surface (Larson et al., 2008). For cryospheric monitoring, GNSS-IR leverages the dramatic dielectric contrast between liquid seawater ($\varepsilon \approx 70 + 64i$) and sea ice ($\varepsilon \approx 3.0 + 0.004i$) at L-band frequencies (~1.5 GHz), causing distinct

https://doi.org/10.5194/egusphere-2026-1160
Preprint. Discussion started: 20 May 2026

variations in the Signal-to-Noise Ratio (SNR) as the surface state changes (Hallikainen and Winebrenner, 1992; Zavorotny et al., 2014). Since the pioneering work on snow depth retrieval (Larson et al., 2009), the technique has been successfully adapted for cryospheric applications, including sea ice characterization (Fabra et al., 2012; Munoz-Martin et al., 2020; Semmling et al., 2019; Xie, 2022) and lake ice phenology (Ghiasi et al., 2020; D. Jacobson, 2015; Du et al., 2017). More recently, Song et al., (2022) introduced the Amplitude Integration Factor (AIF) method, which integrates reflected signal power to provide a robust metric for ice-water discrimination.

However, utilizing sub-kilometer GNSS-IR observations for climate monitoring is hindered by hardware discontinuities (e.g., receiver upgrades) that alter signal magnitudes and obscure multi-decadal trends. Overcoming these observational limits, this study leverages a continuous, 20-year (2003–2023) high-resolution dataset from Tuktoyaktuk in the Beaufort Sea. Moving beyond a technical retrieval method, our primary objective is to investigate the long-term evolution and physical drivers of coastal sea ice phenology.

Specifically, we aim to: (1) capture fine-scale freeze-thaw dynamics, particularly initial nearshore frazil ice formation invisible to coarse-resolution imagery; (2) quantify long-term phenological trends and characterize the pronounced asymmetric decline in ice season duration ; and (3) elucidate the physical mechanisms driving these shifts by examining localized responses to thermal forcings and the impact of extreme meteorological anomalies (e.g., the anomalous 2018 ice year).

2 Study Area and Datasets

2.1 Cryospheric Context of the Tuktoyaktuk Coast

This study utilizes observations from the Tuktoyaktuk (TUKT) station (69.4382°N, 132.9943°W), located on a low-lying peninsula along the Beaufort Sea coast in the western Canadian Arctic. The regional climate is classified as polar tundra, with a mean annual temperature of approximately −9 °C(Environment and Climate Change Canada, 2024). The Beaufort Sea coastal zone is a critical hotspot for Arctic climate change, where the lengthening of the open-water season and increased oceanic heat uptake have profoundly altered the local energy budget. The local ice regime is characterized by a prolonged landfast ice season. Sea ice typically begins to form in late September to early October and persists until late June, with maximum thermodynamic growth reaching 1.5–2.0 m in thickness(Canada et al., 2012). The semi-enclosed bay geometry at TUKT promotes earlier freeze-up compared to more exposed coastal locations, while the stable landfast ice provides a platform for substantial snow accumulation (20–80 cm depth)(Palmer et al., 2012). This setting represents a natural laboratory for monitoring complex coastal sea ice phenology. Understanding the high-resolution freeze-thaw dynamics here is critical, as shifts in landfast ice phenology directly dictate the coastline's exposure to autumn storm surges and thermal abrasion, which significantly accelerate permafrost erosion in this region.

https://doi.org/10.5194/egusphere-2026-1160
Preprint. Discussion started: 20 May 2026

2.2 Long-term GNSS Observations

The primary dataset is derived from the continuous GNSS observations at the TUKT station, operated by Natural Resources Canada as part of the Canadian Active Control System (CACS). The site provides a continuous 20-year observation span from 2003-08-21 to 2023-09-06, boasting a high data completeness of 97.5 % (7,136 available days). The GNSS choke ring antenna (ASH701945E_M) is mounted on a stable pillar approximately 6 m above mean sea level.

For GNSS-IR cryospheric sensing, observations were strictly confined to satellite tracks with elevation angles of 5°–15° and azimuth angles of 8°–125°. This specific geometry ensures that the reflection footprints—defined by the First Fresnel Zones—are entirely cast over the nearshore ocean surface rather than terrestrial permafrost (Fig. 1). Depending on the elevation angle, the spatial footprint ranges from approximately 8 m to 40 m in radius (50–400 m²). These spatial scales are one to two orders of magnitude finer than operational passive microwave satellite products, uniquely enabling the resolution of sub-kilometer nearshore ice dynamics.

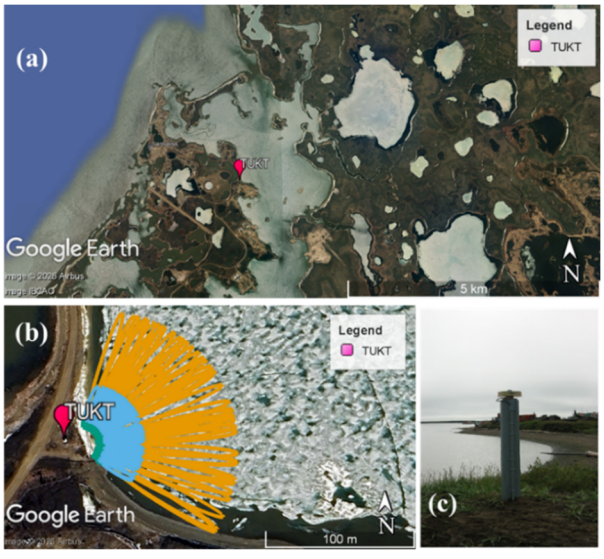

Figure 1. (a) Location of TUKT GNSS station in Tuktoyaktuk, Northwest Territories, Canada, on the Beaufort Sea coast (red point). **(b)** First Fresnel zones (ellipses) for elevation angles of 5° (green), 10° (sky blue), and 15° (orange) showing the spatial extent of the reflection footprint. The Fresnel zones were generated using the GNSS-IR Reflection Zone Mapping tool (version 2.0, https://gnss-reflections.org/rzones). **(c)** Photograph of the TUKT GNSS station showing the choke ring antenna on the monument. Sources: Google Earth imagery and SONEL database (https://www.sonel.org).

Maintaining a multi-decadal observation record inevitably involves hardware maintenance. Throughout the 20-year period, the station underwent several receiver upgrades, with the most significant occurring on 2015-12-16 (an upgrade to the Trimble NETR9 receiver). This specific hardware change resulted in improved signal tracking but introduced a ~27 % reduction in the absolute magnitude of the reflected signal due to enhanced multipath suppression. Overcoming this decadal

https://doi.org/10.5194/egusphere-2026-1160
Preprint. Discussion started: 20 May 2026

hardware-induced discontinuity to extract a physically consistent climate record is a primary methodological focus of this study (detailed in Sect. 3).

2.3 Auxiliary Datasets for Thermodynamic and Spatial Analysis

To investigate the physical drivers of the detected phenological shifts and to evaluate spatial heterogeneity, we integrate four complementary datasets spanning different physical principles and spatial scales (Table 1).

Table 1. Summary of datasets used in this study

Data Source	Spatial Resolution	Temporal Resolution	Period	Completeness	Primary Application
TUKT GNSS	~100 m	Hourly	2003-2023	97 %	AIF calculation, phenology detection
IMS	4 km	Daily	2004-2023	100 %	Validation of phenology dates
ERA5	28 km	Hourly	2003-2023	100 %	Validation and analysis (FDD/TDD)
NAVCAN	Point	Hourly	2003-2023	92 %	Local weather ground-truth
Sentinel-2	10 m	5 days	-	-	Visual validation of ice conditions

All datasets are publicly available: GNSS data from SONEL (https://www.sonel.org), IMS from NSIDC (https://nsidc.org/data/g02156), ERA5 from Copernicus Climate Data Store (https://cds.climate.copernicus.eu), meteorological data from Environment Canada archives, and Sentinel-2 from Copernicus Data Space (https://dataspace.copernicus.eu).

2.3.1 ECMWF ERA5 Reanalysis

Meteorological variables (2-m air temperature, sea surface temperature, and ice surface temperature) were extracted from the ERA5 reanalysis. Validated against local in-situ data (R = 99.1 %, RMSE = 1.98 °C) , these fields are utilized to verify thermodynamic thresholds and calculate accumulated Freezing Degree-Days (FDD) and Thawing Degree-Days (TDD) for driving mechanism analysis.

2.3.2 IMS Daily Snow and Ice Products

The Interactive Multisensor Snow and Ice Mapping System (IMS) provides an independent spatial reference. We define regional ice presence using an 11×11 pixel window (~44×44 km) centered on the GNSS station with an ice probability threshold of $\geqslant 0.5$. This comparison quantifies scale-dependent observation biases, particularly the temporal lag of coarse-resolution sensors in resolving initial frazil ice.

https://doi.org/10.5194/egusphere-2026-1160
Preprint. Discussion started: 20 May 2026

2.3.3 In-Situ Meteorological Observations

Surface observations from the Tuktoyaktuk Airport station (1.3 km from the GNSS antenna) serve as the primary local thermodynamic reference. These records verify short-term signal variability, ensuring rapid GNSS-IR fluctuations are correctly attributed to true physical phase transitions rather than weather-driven noise. To guarantee rigorous physical consistency, all timestamps across datasets are strictly standardized to Coordinated Universal Time (UTC).

2.3.4 Sentinel-2 Optical Imagery

Multispectral optical imagery from Sentinel-2 is employed for targeted visual validation. Cloud-free scenes are leveraged exclusively during critical transition periods to unambiguously resolve complex ice-water mixed states (e.g., melt ponds vs. open leads) within the GNSS-IR reflection footprint that confound coarser data.

3 Methodology

3.1 GNSS-IR Principles and Theoretical Basis for Sea Ice Detection

3.1.1 Basic GNSS-IR Interference Principles

GNSS-IR infers surface properties by exploiting the interference between direct line-of-sight GNSS signals and those reflected from the near-surface (e.g., ocean or ice). Because geodetic antennas imperfectly reject low-elevation multipath, they capture these reflected signals alongside the dominant direct signal (Larson et al., 2008). As illustrated in Figure 2, the elevation-dependent path length difference between these two components creates a phase offset, which manifests as observable oscillations in the Signal-to-Noise Ratio (SNR).

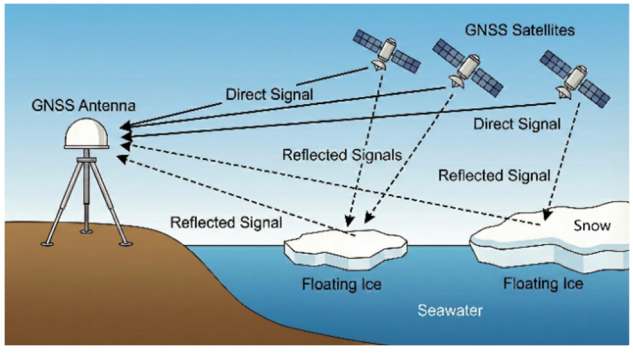

Figure 2. Schematic diagram of inversion of near-surface parameters from GNSS reflected interference signals

After removing the low-frequency trend dominated by the direct signal, the oscillatory interference component, known as the residual SNR $dSNR$), can be expressed as (Larson et al., 2008; Nievinski and Larson, 2014):

$$dSNR \propto \left|\frac{V_{dir}V_{ref}}{V_n^2}\right| \cos\left(\psi_{ref}(\theta)\right) \propto \vartheta^{ant}(\theta)\vartheta^{ant}(\theta_{ref})\Re_{ref}^{RL}(\theta)\Upsilon(\theta, s_h)\cos\left(\psi_{ref}(\theta)\right) \quad (1)$$

https://doi.org/10.5194/egusphere-2026-1160
Preprint. Discussion started: 20 May 2026

where ϑ^{ant} is the antenna gain pattern, $\Re_{ref}^{RL}$ is the Fresnel reflection coefficient for right-hand circularly polarized signals, $\Upsilon(\theta, s_h)$ represents power attenuation due to surface roughness (s_h) (Strandberg et al., 2017; Ulaby et al., 2014), and ψ_{ref} is the multipath phase difference.

The amplitude envelope of these $dSNR$ oscillations, $A(\theta)$, provides a direct measure of the reflected signal power reaching the antenna. Based on the decomposition of the interference signal, this amplitude is proportional to the key surface and geometric parameters:

$$A(\theta) \propto \vartheta^{ant}(\theta)\vartheta^{ant}(\theta_{ref})\sqrt{\Re_{ref}^{RL}(\theta)}\Upsilon(\theta, s_h) \quad (2)$$

3.1.2 Theoretical Basis for Sea Ice Detection

The fundamental principle enabling GNSS-IR sea ice detection is the stark dielectric contrast between seawater and sea ice at L-band frequencies (~1.5 GHz). Seawater's high salinity yields a complex permittivity with substantial dielectric loss ($\varepsilon_{\text{seawater}} = 70 + 64i$ at 0°C) (Ulaby et al., 2014). Conversely, first-year sea ice behaves electromagnetically similar to freshwater ice ($\varepsilon_{\text{ice}} \approx 3.0 + 0.004i$) with minimal L-band interference from dry snow (Hallikainen and Winebrenner, 1992; Semmling et al., 2022). The presence of dry snow on sea ice typically has minimal effect on L-band reflectivity due to its low permittivity(Cardellach et al., 2012). Thus, the real part (permittivity) differs by a factor of ~23, and the imaginary part (loss factor) by over three orders of magnitude.

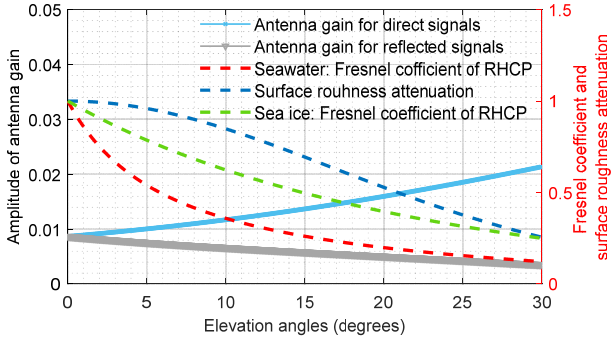

Figure 3. Decomposition of factors controlling reflected signal amplitude. While antenna gains (solid lines) and surface roughness attenuation (blue dashed line) similarly affect both media, the Fresnel reflection coefficient is substantially higher for sea ice (green dashed) than seawater (red dashed) across all elevation angles, driving the dominant amplitude difference.

Following Equation (2), this profound dielectric contrast dictates the Fresnel reflection coefficients and the received signal amplitude. As explicitly decomposed in Figure 3, while antenna gain and surface roughness uniformly attenuate signals across both media, the Fresnel reflection coefficient acts as the dominant physical driver of amplitude divergence. At a 5° elevation angle, the reflectivity for ice is ~23 versus ~0.22 for seawater, representing a ~45 % increase. Consequently, the

https://doi.org/10.5194/egusphere-2026-1160
Preprint. Discussion started: 20 May 2026

reflected signal amplitude from ice consistently exceeds that of water by a factor of 2–3 across the entire operational elevation range (5–15°), providing an unambiguous physical basis for surface state discrimination.

3.2 The Amplitude Integration Factor (AIF) as a Physical Proxy

Relying on single-angle amplitude observations can be susceptible to localized high-frequency noise. To extract a robust climate metric, we employ the Amplitude Integration Factor (AIF), which quantifies the cumulative reflected power across the operational elevation angle range.

Following a continuous wavelet transform (CWT) to extract the elevation-dependent amplitude curve $P_{RH}(t, N, \theta)$, the AIF for satellite N at time t is mathematically defined as:

$$\Lambda(t, N) = \frac{\pi}{180} \int_{\theta_{\min}}^{\theta_{\max}} P_{RH}(t, N, \theta)\, d\theta \approx \frac{\pi}{180} \sum_{i=1}^{n} \Delta\theta_i \cdot P_{RH}(t, N, \theta_i) \quad (3)$$

where $\theta_{\min}$ and $\theta_{\max}$ define the elevation angle range (5° and 15° in this study), n is the number of discrete elevation angle samples, $\pi/180$ converts degrees to radians for dimensional consistency. Physically, $\Lambda(t, N)$ integrates both the increased absolute magnitude of reflection and the altered angular decay characteristics of the ice surface, producing a metric that is substantially larger for ice-covered surfaces compared to open water.

For the TUKT station (nominal height ~ 6 m above sea level), we use scales corresponding to heights from $H_{Rh} - 3\sigma_{Rh}$ to $H_{Rh} + 3\sigma_{Rh}$, where $\sigma_{Rh} \approx 0.2$ m accounts for uncertainty. The amplitude curve $P_{RH}(t, N, \theta)$ is estimated by averaging wavelet power $WT_f^{\varpi}(\theta)$ across the height(h) range:

$$P_{RH}(t, N, \theta) = \langle WT_f^{\varpi}(h, \theta) \rangle, h \in [H_{Rh} - 3\sigma_{Rh}, H_{Rh} + 3\sigma_{Rh}] \quad (4)$$

This procedure effectively filters high-frequency noise while preserving the elevation-dependent amplitude trend. The amplitude curve is then sampled at $n \approx 800$ discrete elevation angles via cubic spline interpolation to ensure uniform sampling across all satellite tracks, followed by a 3-point moving average to further reduce noise.

3.3 Decadal Inter-calibration and Phenological Detection

3.3.1 Inter-calibration and Data Homogenization

Prior to decadal inter-calibration, a rigorous quality control protocol is applied to individual AIF observations to eliminate spurious multipath artifacts. Observations are excluded if they fail to span the complete operational elevation range (5-15°), exhibit a satellite track duration of less than one hour, or display ambiguous reflection signatures in the Lomb-Scargle periodogram (e.g., maximum spectral amplitude < 8 or peak-to-noise ratio < 1.5). This robust physical screening retains approximately 90 % of the highest-quality observations for subsequent climate analysis.

Transitioning this filtered dataset into a 20-year Climate Data Record requires overcoming inevitable hardware discontinuities. Notably, a major receiver upgrade at the TUKT station on 2015-12-16 (Ashtech MicroZ to Trimble NETR9) introduced an enhanced multipath suppression mechanism, resulting in an artificial reduction of approximately 27 % in the absolute magnitude of the raw AIF. In addition, raw AIF values vary inherently among satellites due to specific transmission

https://doi.org/10.5194/egusphere-2026-1160
Preprint. Discussion started: 20 May 2026

powers and orbital geometries. To homogenize the record and enable the combination of all observations into a unified time series, we apply an inter-satellite and inter-annual reference period normalization:

$$\Lambda^c(t,N) = \Lambda(t,N) - \Lambda_m^{t_1,t_2}(N) \quad (5)$$

where Λ^c is the calibrated AIF and $\Lambda_m^{t_1,t_2}(N)$ is the mean AIF for satellite N during the reference period $[t_1, t_2]$.

For the TUKT station, we utilize the consistently ice-free summer period (Day of Year (DOY) 200–250) as the thermodynamic baseline. Setting the calibrated AIF to zero-mean during these dates ensures that positive Λ^c values indicate enhanced reflection relative to open water conditions, directly corresponding to ice or snow presence. Because the hardware-induced attenuation proportionally scales down both the ice signal and the summer baseline noise, this normalization ensures the relative Signal-to-Noise Ratio remains decadal consistent.

To mitigate residual periodic fluctuations driven by orbital repeat cycles, the calibrated time series is smoothed using a third-order Butterworth low-pass filter (cutoff frequency: 0.5 cycles day^{-1}). Compared to conventional smoothing techniques (e.g., moving average), this specific filtering strategy effectively attenuates high-frequency noise while preserving the sharp physical signal transitions triggered by sudden sea ice formation.

3.3.2 Phenological Transition Date Detection

To assess reference period stability, we computed year-to-year variance in mean calibrated AIF during DOY 200-250:

$$\sigma_{ref} = 0.19 \text{ (in units of calibrated AIF)} \quad (6)$$

Compared to the typical winter seasonal signal amplitude of 3.89 (DOY 300–365), this baseline variability (σ_{ref}) represents merely ~4.8 % of the signal, confirming it is exceptionally stable for decadal climate trend detection. Phenological transition dates (ice-out and freeze-up) are determined using a semi-automated approach based on the calibrated and low-pass filtered AIF time series. The detection threshold is defined as $\eta_{\mathrm{th}} = 3\sigma_{\mathrm{ref}}$. This rigorous criterion identifies significant physical deviations from the baseline open-water variability. Crucially, because this threshold is dynamically derived from σ_{ref} rather than a fixed constant, it inherently adapts to the post-2015 signal compression, preventing any artificial delays in phenological detection.

To account for transient freeze-thaw cycles often observed during transition periods, we adopted the following criteria to rigorously define the timing of stable ice cover and continuous open water:

- **Ice-out Date (Start of Open Water):** Defined as the latest date when the AIF drops below the threshold ($3\sigma_{ref}$) and establishes a sustained low value. This criterion ensures that the date marks the definitive end of the ice season, inclusive of any late-stage refreezing events.
- **Freeze-up Date (Start of Ice Season):** Defined as the earliest date when the AIF rises above $3\sigma_{ref}$ and maintains a sustained high value for at least 5 days. This captures the initial onset of stable ice formation, treating subsequent minor thawing events as part of the established winter ice season.

https://doi.org/10.5194/egusphere-2026-1160
Preprint. Discussion started: 20 May 2026

A threshold sensitivity analysis (varying $3\sigma_{ref}$ by 10 %) indicated that the uncertainty in the phenological dates is approximately 1~2 days, which is well below the observed interannual variability.

4 Results and Discussions

4.1 Annual AIF Cycle and Phenological Transitions: Case of 2019

To establish the physical basis and detection capability of the calibrated Amplitude Integration Factor (AIF) methodology, we conducted a comprehensive multi-source analysis using the continuous 2019 time series as a reference case. By integrating the sub-kilometer AIF proxy with ERA5 reanalysis fields, in-situ meteorological observations, and high-resolution Sentinel-2 optical imagery, we elucidate how the GNSS reflection signal responds dynamically to complex coastal thermodynamic forcing.

The complete 2019 AIF time series reveals a distinct cyclic pattern that corresponds precisely to the known physical evolution of the seasonal coastal ice regime (Fig. 4 and Fig. 5). We identify five distinct thermodynamic phases:

Phase I (Stable Winter, DOY 1-130): The AIF maintains a high magnitude, reflecting the low complex permittivity of the consolidated landfast ice. A gradual decline from approximately 4.1 to 0.8 is observed. This progressive attenuation corresponds to continuous snow densification and destructive metamorphism on the ice surface, which gradually increases surface roughness and volume scattering.

Phase II (Melt Onset, DOY 131-146): A distinct, counter-intuitive rebound in the AIF (peaking at ~2.7) occurs. As validated by ERA5 data (Fig. 5), this perfectly coincides with the period when surface air temperatures first persistently exceed -1.6°C. This signal spike physically represents the initial exposure of highly reflective bare ice or the formation of shallow melt ponds beneath the decaying snowpack, creating sharp localized dielectric contrasts.

Phase III (Advanced Melt, DOY 147-162): A secondary, steep decline in the AIF ensues. During this phase, extensive meltwater layers develop and the ice structure begins to disintegrate, sharply attenuating the reflection coefficient through increased surface roughness and dielectric loss.

Phase IV (Open Water, DOY 163-288): The AIF reaches and sustains its minimum baseline (approximately 0.0 ± 0.2), strictly indicating stable ice-free conditions. Brief, minor fluctuations during this summer period correlate directly with high wind events (>25 m s^{-1}) in the ERA5 record, which temporarily increase sea surface roughness.

Phase V (Freeze-up, DOY 289-365): A sharp, almost instantaneous AIF surge marks the autumn freeze-up transition. This is immediately followed by sustained high values (> 3) as the newly formed ice consolidates and dielectric loss plummets.

https://doi.org/10.5194/egusphere-2026-1160
Preprint. Discussion started: 20 May 2026

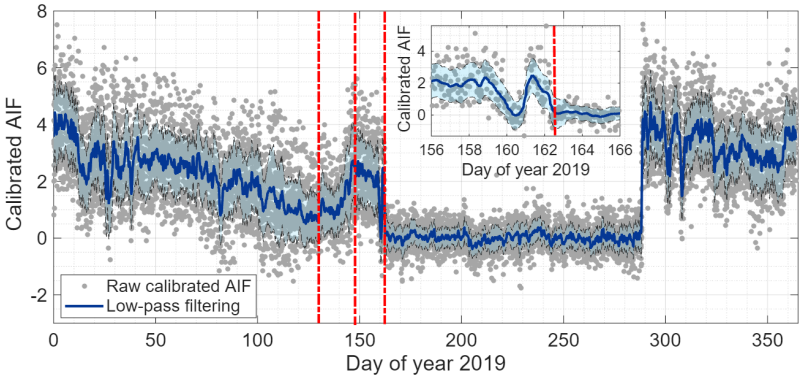

Figure 4. Annual evolution of calibrated AIF for 2019 with multi-source validation. Gray points: raw AIF from individual satellite tracks; blue line: low-pass filtering; cyan shading: $\pm 1\sigma$ uncertainty.

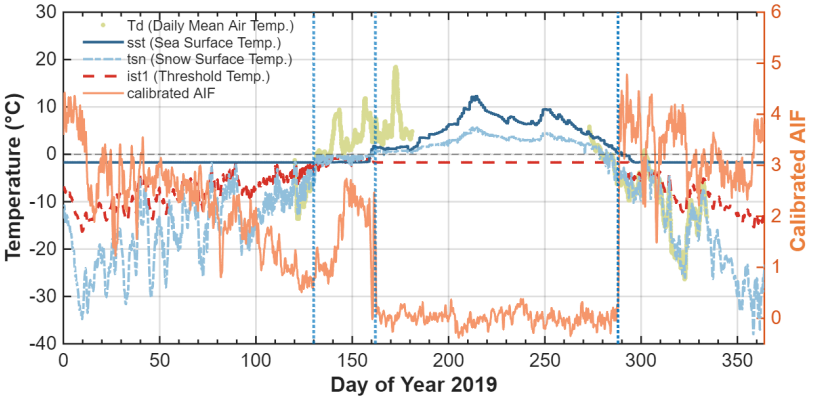

Figure 5. Multi-source validation of 2019 phenological transitions. Time series of calibrated AIF (orange line, right axis) overlaid with meteorological variables (left axis) including air temperature (in-situ (Td: daily) and ERA5), sea surface temperature (sst), and ice surface temperature (ist) from ERA5. Vertical dashed lines indicate key transition periods detected by AIF methods.

While the temporal progression of the AIF aligns exceptionally well with the ERA5-derived Sea Surface Temperature (SST) and Ice Surface Temperature (IST), specific systematic discrepancies emerge when comparing exact transition dates across different datasets (Table 2). These discrepancies highlight the scale-dependent nature of coastal ice observation.

Table 2. Comparison of 2019 phenological transition dates from multiple independent data sources.

Method	Ice-out (DOY)	Freeze-up (DOY)	Spatial Resolution
GNSS-IR (this study)	162	289	~100 m footprint
ERA5 IST	161	293	28 km grid

https://doi.org/10.5194/egusphere-2026-1160
Preprint. Discussion started: 20 May 2026

Method	Ice-out (DOY)	Freeze-up (DOY)	Spatial Resolution
IMS	161	291	4 km grid
Sentinel-2 (visual)	161-162	289	10 m resolution

For the spring ice-out, the methods show strong convergence. GNSS-IR detects the final transition to open water on DOY 162, while ERA5 and the 4-km IMS product indicate ice absence on DOY 161. Cloud-free Sentinel-2 imagery (10 m resolution) from DOY 160 reveals severe ice cracking and only small remnants of ice persisting within the semi-enclosed bay (Fig. 6(a-c)). This 1-to-2 day difference falls within the natural spatial heterogeneity of the decaying ice pack.

Conversely, the autumn freeze-up exposes a profound observational divergence. GNSS-IR detects the freeze-up transition on DOY 289, driven by in-situ air temperatures plunging to -6.1°C. However, the ERA5 IST fields do not register stable ice presence until DOY 293 (a 4-day lag), and the operational IMS product delays detection until DOY 291.

(a) Satellite image at TUKT station on DOY 159 (2019-06-08)

(b) Satellite image at TUKT station on DOY 160 (2019-06-09)

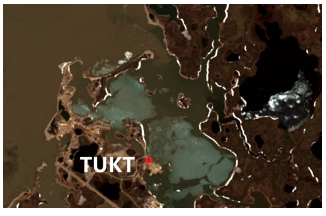

(c) Satellite image at TUKT station on DOY 160 (zoom out for (b))

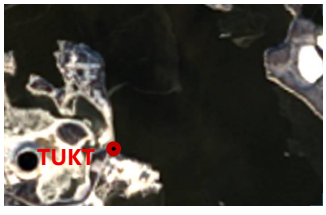

(d) Satellite image at TUKT station on DOY 288 (2019-10-15)

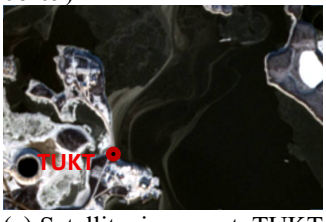

(e) Satellite image at TUKT station on DOY 289 (2019-10-16)

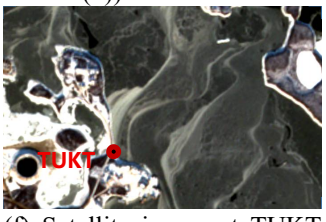

(f) Satellite image at TUKT station on DOY 293 (2019-10-20)

Figure 6. Sentinel-2 validation (10 m resolution) of sea ice transitions at TUKT station (red star). Ice-out: **(a)** DOY 159: residual ice 80-90 %; **(b)** DOY 160: residual ice 60-80 %, obvious cracks in sea ice have emerged; **(c)** DOY 160 zoom-in of (b): only remnants of sea ice were observed within the enclosed bay. Freeze-up: **(d)** DOY 288: initial ice formation 10-20 % in upper-left nearshore zone; **(e)** DOY 289: consolidation 40-60 %; **(f)** DOY 293: complete coverage. Contains modified Copernicus Sentinel data [2019].

The Sentinel-2 optical imagery sequence provides the ultimate ground-truth resolution for this discrepancy. On DOY 288, initial frazil ice formation (10 %–20 % concentration) is visually confirmed in the immediate nearshore zone (Fig. 6(d)). By

https://doi.org/10.5194/egusphere-2026-1160
Preprint. Discussion started: 20 May 2026

DOY 289—the exact date of the GNSS-IR detection—ice concentration rapidly increases to 40 %–60 % within the GNSS reflection footprint (Fig. 6(e)). Complete, basin-wide ice coverage is not visually confirmed until DOY 293 (Fig. 6(f)), perfectly coinciding with the delayed ERA5 and IMS detection dates.

This high-resolution cross-validation conclusively demonstrates that the localized GNSS-IR footprint (< 100 m) accurately resolves the genuine initial formation of nearshore frazil ice. In contrast, coarser-resolution satellite and reanalysis products systematically suffer from a "temporal lag," requiring extensive, bay-wide ice consolidation before their large spatial grids register the phase transition. This confirms the unique capability of GNSS-IR to capture sub-grid thermodynamic processes in the coastal boundary zone.

4.2 The 20-Year Climatology and Asymmetric Decline

4.2.1 20-Year Phenological Statistics

Leveraging the decadal stability of the calibrated AIF proxy, we established a continuous 20-year (2003–2023) coastal sea ice climatology for the Tuktoyaktuk station (Fig. 7). Representing the longest continuous ground-based GNSS-IR sea ice dataset published to date, the record spans from late 2003 through 2023, providing 19 complete annual ice cycles. Crucially, as a direct result of the inter-annual reference period normalization implemented in Sect. 3.3, this calibrated record seamlessly bridges the major receiver upgrade on 2015-12-16. The systematic baseline shift (a 27 % reduction in absolute magnitude) and varying noise levels associated with the hardware change were successfully neutralized. This ensures that the characteristic signal variations corresponding to distinct phenological events are preserved with strict physical consistency throughout the two decades, avoiding the introduction of artificial climatic jumps.

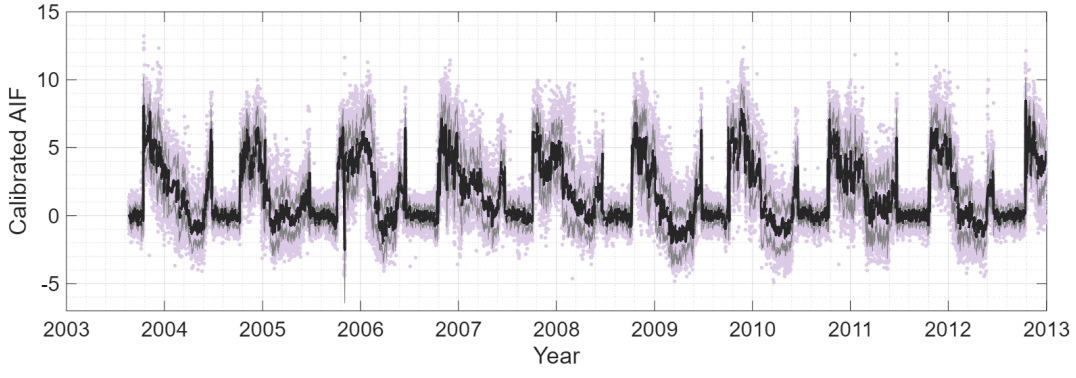

(a) calibrated AIF for year 2003 through 2012

https://doi.org/10.5194/egusphere-2026-1160
Preprint. Discussion started: 20 May 2026

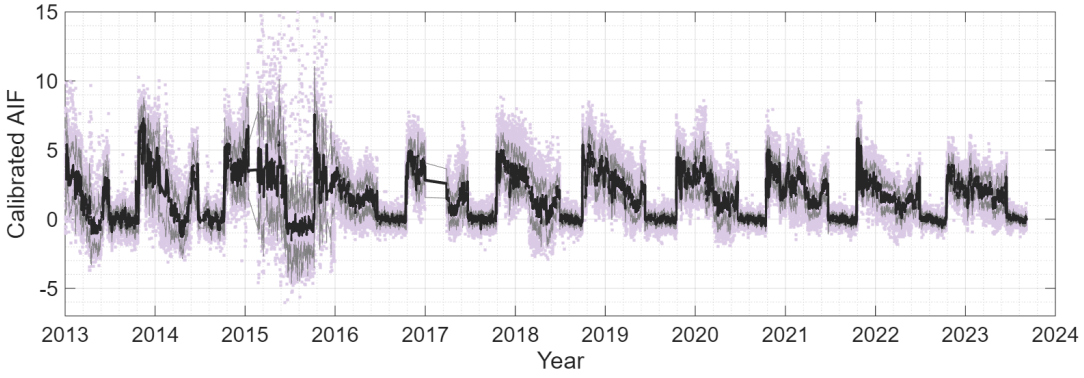

(b) calibrated AIF for year 2013 through 2023

Figure 7. Complete 20-year calibrated AIF record (2003–2023) at the TUKT station for (a) 2003–2012 and (b) 2013–2023. Light purple points indicate individual satellite observations, overlaid with a filtered AIF (black line) and ±1σ uncertainty envelope (gray shading).

The extracted phenological metrics (Table 3) maintain an exceptional 97 % data completeness, with zero observational gaps during the critical transition periods from 2004 through 2022. Across the complete 19-year record, the mean ice-out occurs at DOY 173.1 ± 4.5, and the mean freeze-up at DOY 284.1 ± 6.5. This establishes a mean within-year ice duration of 254.1 ± 8.6 days and an ice-free period of 110.9 ± 8.6 days. These statistics provide a critical baseline for characterizing the typical thermodynamic regime of the Beaufort Sea coastal zone.

Table 3. Sea ice phenology metrics extracted from the calibrated AIF time series (2003–2023). Transition dates are reported in Day of Year (DOY). While Ice duration denotes the frozen period within a nominal calendar year, Corrected ice duration spans the continuous freeze-to-thaw cycle (from the previous year's freeze-up to the current year's ice-out) to accurately reflect the true physical ice season length.

Year	Ice-out date	Freeze-up date	Ice-free duration	Ice duration	Corrected ice duration
2003	/	286.86	/	/	/
2004	177.57	282.29	104.72	260.28	255.71
2005	176.36	278.45	102.08	262.92	260.07
2006	169.78	286.18	116.40	248.60	256.34
2007	172.83	276.20	103.37	261.63	251.65
2008	174.37	282.50	108.13	256.87	263.16
2009	175.92	272.21	96.29	268.71	259.42
2010	169.64	281.06	111.42	253.58	262.43
2011	174.08	292.37	118.29	246.71	258.02
2012	169.28	287.21	117.92	247.08	241.91
2013	176.97	297.61	120.64	244.36	255.76

https://doi.org/10.5194/egusphere-2026-1160
Preprint. Discussion started: 20 May 2026

2014	174.75	282.15	107.41	257.59	242.14
2015	166.68	280.15	113.47	251.53	249.52
2016	170.49	287.66	117.17	247.83	255.34
2017	171.84	286.82	114.98	250.02	250.18
2018	180.57	272.19	91.62	273.38	258.75
2019	162.51	288.27	125.76	239.24	255.32
2020	173.98	286.69	112.71	252.29	250.71
2021	172.48	289.23	116.75	248.25	251.79
2022	179.60	287.94	108.33	256.67	255.37
2023	167.68	/	/	/	244.75

The standard deviations indicate profound interannual variability, which is distinctly bounded by two extreme years. The year 2019 experienced the earliest ice-out (DOY 162.5) and one of the latest freeze-up dates, resulting in the shortest ice duration on record (239.2 days). Conversely, 2018 represents an extreme meteorological anomaly, characterized by the latest ice-out (DOY 180.6) combined with an anomalously early freeze-up (DOY 272.2), producing the longest recorded ice duration (273.4 days).

Finally, to rigorously assess climate trends without the artificial segmentation of calendar years, we computed a "corrected ice duration" (Table 3). By calculating the continuous span from the previous year's freeze-up to the current year's ice-out, this metric captures the true, uninterrupted physical freeze-to-thaw cycle. The mean corrected ice duration is 253.9 ± 6.25 days, ranging from 241.9 days (2011–2012) to 263.2 days (2007–2008). This cross-year calculation provides a far more robust and physically meaningful basis for identifying genuine climatological shifts in the subsequent trend analysis.

4.2.2 Long-Term Trends Analysis

To quantify systematic changes in the coastal sea ice regime, we applied linear regression analysis to the complete continuous record from 2004 through 2023, as shown in Table 4 and Fig. 8.

Table 4. Linear trends in sea ice phenology metrics from GNSS-IR observations at TUKT station (2004 through 2023). Trend rates are reported as days per decade with 95 % confidence intervals.

Metric	With 2018			Without 2018		
	Trend	Detrend STD	*p*	Trend	Detrend STD	*p*
Ice-out date	−1.42	±4.32	0.35	−2.16	±4.24	0.19
Freeze-up date	+3.40	±6.00	0.18	+3.71	±5.21	0.07
Ice duration	−5.40	±8. 04	0.21	−6.41	±6.31	0.08
Ice-free period	+5.40	±8.04	0.21	+6.41	±6.31	0.08
Corrected ice duration	−4.19	±5.43	0.06	−4.63	±5.34	0.04

https://doi.org/10.5194/egusphere-2026-1160
Preprint. Discussion started: 20 May 2026

When evaluating the full 20-year dataset, the profound interannual variability tempers the statistical significance of the long-term trends at the 95 % confidence level ($p < 0.05$). Nevertheless, clear directional trajectories emerge: spring ice-out exhibits a weak advancing trend of -1.42 ± 4.32 days per decade ($p = 0.35$), while autumn freeze-up displays a pronounced delay of $+3.40 \pm 6.00$ days per decade ($p = 0.18$). These combined shifts drive an overall reduction in the within-year ice duration of -5.40 ± 8.04 days per decade ($p = 0.21$).

As highlighted in the statistical baseline, the year 2018 represents an extreme meteorological anomaly (latest ice-out on DOY 180.6 and earliest freeze-up on DOY 272.2), exerting substantial leverage on the regression models. To uncover the underlying climatological trajectory without the dampening effect of this single extreme outlier, we evaluated the trends with 2018 excluded. Under this scenario, the directional trends intensify considerably. The shortening of the ice duration accelerates to -6.41 ± 6.31 days per decade ($p = 0.08$), driven primarily by an exacerbated delay in freeze-up ($+3.71 \pm 5.21$ days per decade, $p = 0.07$). Over the two decades, this underlying trajectory translates to a cumulative reduction of approximately 12.8 days in the coastal ice season.

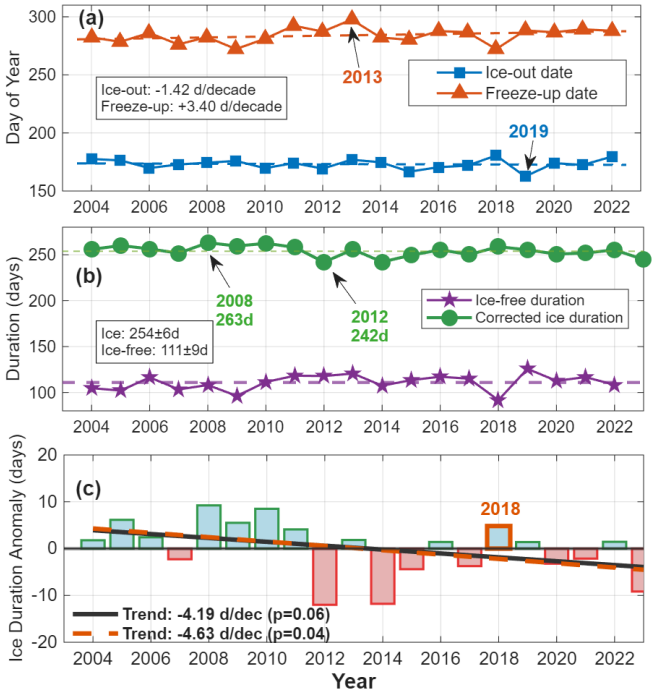

Figure 8. Long-term trends in sea ice phenology from GNSS-IR observations at TUKT station (2004 through 2022). **(a)** Ice-out dates (blue squares) and freeze-up dates (red triangles) with linear trend lines. **(b)** Corrected ice duration (green circles) and ice-free period (purple pentagrams); horizontal dashed lines indicate 19-year means. **(c)** Corrected ice duration anomalies with trend lines for all data (black solid) and excluding 2018 (orange dashed); positive anomalies in light blue, negative in light red. The 2018 data point is highlighted with an orange border.

https://doi.org/10.5194/egusphere-2026-1160
Preprint. Discussion started: 20 May 2026

Crucially, to rigorously eliminate the artificial segmentation of calendar year boundaries, we evaluated the "corrected ice duration," which tracks the continuous, uninterrupted physical freeze-to-thaw cycle. This mathematically robust metric validates the physical meaningfulness of our analytical approach. When the 2018 anomaly is excluded, the corrected ice duration demonstrates a statistically significant shortening trend of −4.63 ± 5.34 days per decade ($p = 0.04$). More importantly, this trend magnitude exhibits remarkable stability, shifting by less than half a day (−4.19 ± 5.43 days per decade, $p = 0.06$) even when the extreme 2018 event is retained. This consistency confirms that the underlying shortening of the ice season (approximately 4–5 days per decade) is a genuine, persistent climatological shift rather than a statistical artifact driven by outlier years. The fact that the trend achieves strict statistical significance ($p < 0.05$) when the extreme noise of 2018 is removed indicates that the climate signal is already detectable, though slightly obscured by localized meteorological extremes.

A critical thermodynamic feature revealed by this trend analysis is the marked asymmetry in both interannual variability and long-term decline. The standard deviation (+6.5 days) and the decadal trend magnitude (+3.40 to +3.71 days per decade for autumn freeze-up substantially exceed those of spring ice-out (± 4.5 days; −1.42 to −2.16 days per decade). This physical asymmetry suggests that the timing of spring ice breakup is relatively deterministic, being tightly coupled to the consistent seasonal increase in solar radiative forcing. In stark contrast, autumn ice formation is highly stochastic and exhibits a heightened sensitivity to climate warming. It is increasingly delayed by a potent "thermal memory" effect, wherein the lengthening summer open-water period facilitates enhanced oceanic heat uptake, which must be fully dissipated to the atmosphere before nearshore frazil ice can successfully consolidate.

4.3 Thermodynamic Drivers of Coastal Sea Ice Phenology

4.3.1 Local Warming Trends and Phenological Coupling

To establish the physical mechanisms governing the long-term phenological shifts, we investigate the regional atmospheric thermal forcing using the strictly UTC-aligned ERA5 reanalysis fields. Having previously established the high reliability of ERA5 against local in-situ observations at Tuktoyaktuk (RMSE = 1.98 °C, r = 0.99), we utilized this dataset to quantify the background climatological warming.

Over the 19-year overlapping record (2004–2022), the annual mean air temperature at the coastal grid cell exhibits profound interannual variability, ranging from -11.75°C in 2004 to -6.52°C in 2019. Despite this intense short-term variability, a statistically significant background warming trend of +1.03 ± 0.44°C per decade ($p = 0.03$) emerges, driving an approximate 1.85°C total temperature increases over the two decades.

This localized warming trend strongly couples with the observed lengthening of the ice-free season (Fig. 9). For the complete dataset, the ice-free duration lengthens at a rate of +5.40 days per decade ($p = 0.21$). However, the relationship is heavily modulated by the extreme 2018 anomaly, which featured a severely constrained ice-free period (91.6 days) despite a relatively warm annual mean temperature (-8.4°C). When this singular dynamic anomaly is excluded, the coupling

https://doi.org/10.5194/egusphere-2026-1160
Preprint. Discussion started: 20 May 2026

strengthens considerably: the lengthening trend of the ice-free duration accelerates to +6.41 days per decade ($p = 0.08$), and the correlation with annual mean temperature improves to $r = 0.56$ ($p = 0.015$).

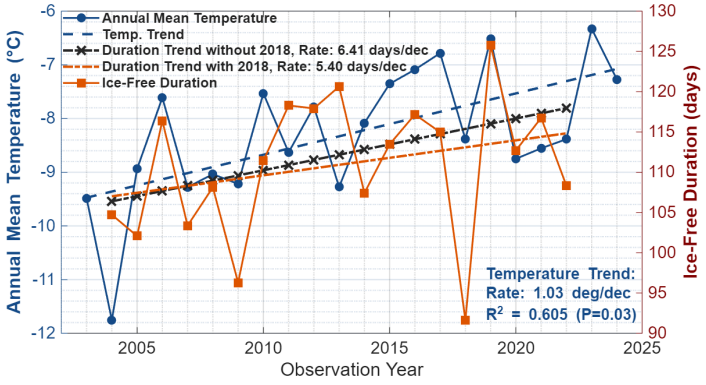

Figure 9. Relationship between annual mean air temperature (ERA5) and ice-free duration. Blue circles with a solid line show annual mean temperature with its linear trend. The orange line with square markers shows the ice-free duration with its corresponding trend. The black dashed line with cross markers indicates the ice-free duration trend excluding the 2018 anomaly.

Despite this robust coupling, the annual mean temperature explains only 32 % of the variance in the ice-free duration ($R^2 = 0.32$). This confirms that while mean atmospheric warming is the primary thermodynamic driver, coastal sea ice phenology is substantially modulated by complex non-thermal dynamic factors—such as wind-driven ice advection, episodic extreme storms, and variations in accumulated snowpack depth—which can temporarily decouple the local surface state from the overarching warming trajectory.

4.3.2 Degree-Day Forcing on Interannual Variability

To further elucidate the physical realism of the GNSS-IR retrieved phenology, we transitioned from annual mean temperatures to cumulative thermal forcing metrics: Thawing Degree-Days (TDD) and Freezing Degree-Days (FDD). Because phase transitions are fundamentally constrained by the latent heat of fusion, analyzing the specific accumulation periods provides deep insights into the timing of surface state changes.

We employed a sliding window approach to identify the effective thermal accumulation periods that exert the strongest linear control over the GNSS-IR detected transition dates (Fig. 10). For spring ice-out, TDD was calculated as the sum of positive daily mean temperatures. The heatmap analysis (Fig. 10(a)) reveals that the strongest negative correlation ($r = -0.81$, $p < 0.001$) occurs within a 3-month accumulation window centered on DOY 128 (early May). This critical window perfectly captures the transitional physics: the period begins with pre-melt snow metamorphism and culminates in the total structural disintegration of the ice pack. The corresponding regression yields a statistically significant coefficient of determination (R^2

https://doi.org/10.5194/egusphere-2026-1160
Preprint. Discussion started: 20 May 2026

= 0.66), demonstrating that GNSS-IR ice-out timing responds predictably to accumulated spring insolation and sensible heat flux.

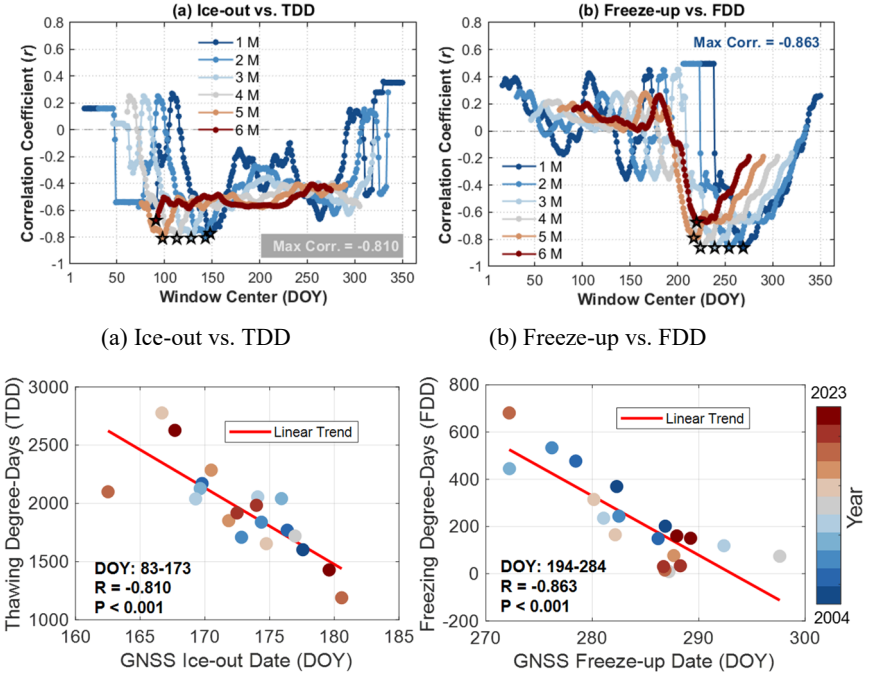

(a) Ice-out vs. TDD (b) Freeze-up vs. FDD

(c) Ice-out date vs. TDD (d) Freeze-up date vs. FDD

Figure 10. Correlation analysis between phenological dates and accumulated thermal forcing. **(a–b)** Heatmaps showing Pearson correlation coefficients (r) as a function of accumulation window center (DOY) and duration (months) for (a) ice-out dates vs. Thawing Degree-Days (TDD) and (b) freeze-up dates vs. Freezing Degree-Days (FDD). White stars denote maximum negative correlations. **(c–d)** Linear regression analysis for the optimal accumulation windows identified in (a) and (b): (c) ice-out vs. TDD and (d) freeze-up vs. FDD.

For the autumn freeze-up, the accumulation of FDD (sum of negative daily mean temperatures) dictates the consolidation process. The optimal integration window (Fig. 10(b)) is identified as a 3-month period centered on DOY 239 (late August). The relationship between this specific FDD window and the GNSS-IR detected freeze-up dates is exceptionally robust ($r = -0.86$, $R^2 = 0.74$, $p < 0.001$).

A crucial physical insight emerges from comparing the two phase transitions: the autumn freeze-up exhibits a substantially higher thermodynamic consistency ($R^2 = 0.74$) than the spring ice-out ($R^2 = 0.66$). This discrepancy perfectly reflects the distinct physical nature of the two boundaries. Freeze-up is an inherently thermodynamic-dominated process governed strictly by progressive oceanic heat loss to the atmosphere. In contrast, while spring melt is initiated by thermal forcing (TDD), the final ice-out event is heavily influenced by mechanical and dynamic forces, such as wind-induced fracturing and

https://doi.org/10.5194/egusphere-2026-1160
Preprint. Discussion started: 20 May 2026

tidal breakup of the weakened ice cover. The ability of the GNSS-IR record to capture these nuanced, thermodynamically distinct physical behaviors serves as the ultimate validation of its long-term climatological reliability.

4.4 Cross-Scale Observational Discrepancies: Resolving Nearshore Frazil Ice

While the preceding thermodynamic analysis validates the temporal accuracy of the GNSS-IR record, comparing these sub-kilometer observations with the operational 4-km IMS satellite product reveals critical insights into the scale-dependent nature of coastal ice dynamics. Rather than mere measurement discrepancies, the systematic differences between GNSS-IR and coarse-resolution satellite data highlight fundamental physical processes occurring at the land-ocean boundary.

Systematic comparison across the 20-year record reveals pronounced, scale-dependent timing offsets (Table 5, Fig. 11). The most profound cross-scale discrepancy emerges during the autumn freeze-up. The highly sensitive GNSS-IR methodology consistently detects the onset of the ice season significantly earlier than the IMS product, exhibiting a mean temporal lead of -5.5 ± 3.7 days. Despite this systematic offset, the GNSS-IR retrieval demonstrates an exceptionally strong and statistically significant interannual correlation with the IMS product ($r = 0.82$, $p < 0.001$).

Table 5. Statistical comparison of phenological timing differences between GNSS-IR and IMS (2004 through 2023). Negative values indicate earlier detection by GNSS-IR.

Transition Type	Mean Offset (GNSS-IR minus IMS, days)	Standard Deviation (days)	Range (days)	Temporal Correlation
Freeze-up	−5.5 (earlier)	±3.7	−12.8 to −0.7	$r = 0.82$ ($p < 0.001$)
Ice-out	−1.4 (later)	±7.5	−14.3 to +9.3	$r = 0.05$ ($p = 0.85$)
Ice duration	+3.8	±6.9	−9.9 to +16.7	$r = 0.64$ ($p < 0.01$)

This systemic offset is expected and physically explainable. As corroborated by the Sentinel-2 visual evidence (Sect. 4.1), the sub-kilometer GNSS-IR footprint immediately captures the initial formation of nearshore frazil ice. Coarse passive microwave and multi-sensor products like IMS suffer from a spatial dilution effect; they require a much larger volume of the 16 km² pixel to consolidate into solid ice to overcome the radiometrically warm signal of the surrounding open ocean. Furthermore, this 5.5-day lead is not solely a resolution artifact, but also reflects genuine local thermodynamics. The shallow, lower-salinity nearshore waters strictly monitored by GNSS-IR cool more rapidly and physically freeze earlier than the deeper, more saline offshore waters encompassed by the broader IMS pixel. Therefore, this −5.5-day lead captures both the earlier onset of nearshore thermodynamic freezing and the subsequent physical interval required for regional ice consolidation across the coarser satellite grid.

https://doi.org/10.5194/egusphere-2026-1160
Preprint. Discussion started: 20 May 2026

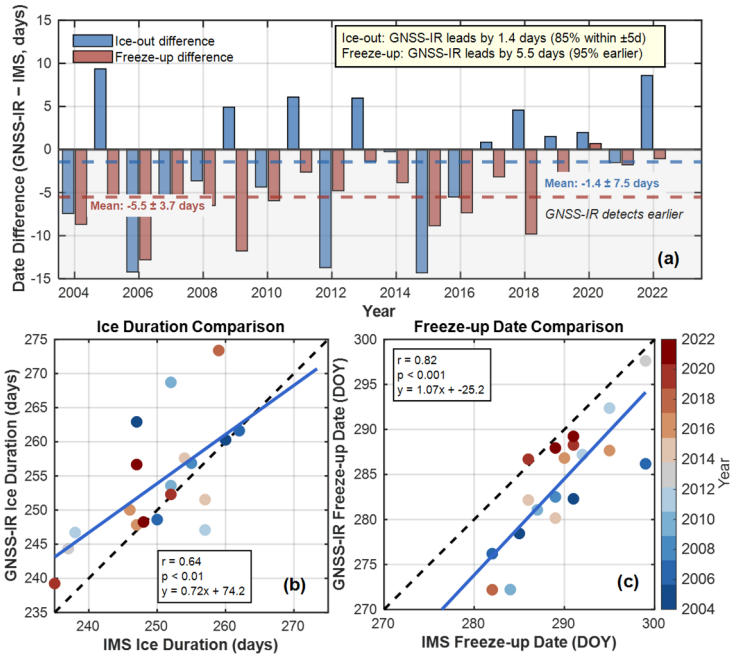

Figure 11. Comparison between GNSS-IR and IMS phenological metrics (2004 through 2023). **(a)** Time series of date differences (GNSS-IR minus IMS). **(b)** Scatter plot of ice duration. **(c)** Scatter plot of freeze-up dates. The black dashed lines represent the 1:1 relationship, while the blue solid lines show linear fits.

Conversely, the spring breakup phase presents a vastly different observational challenge. For ice-out, GNSS-IR detects clearance slightly earlier than IMS, with a mean offset of −1.4 ± 7.5 days. Theoretically, nearshore landfast ice is expected to melt later than offshore pack ice. However, the large standard deviation (± 7.5 days) and the complete lack of temporal correlation ($r = 0.05$, $p = 0.85$) indicate that this mean offset is not a systematic lead, but rather a reflection of extreme spatial heterogeneity. This decoupling physically reflects the chaotic nature of nearshore ablation, where localized fracturing, wind-driven ice advection, and meltwater ponding within the small GNSS reflection zone do not synchronize linearly with the melting dynamics of the broader 4-km satellite grid.

Nevertheless, the aggregate ice season duration maintains a robust correlation between the two platforms ($r = 0.64$, $p < 0.01$). This confirms that despite the localized spatial noise during the spring breakup, the ground-based dataset effectively captures the overarching long-term climatic signal. Ultimately, these timing differences represent physical detection thresholds rather than measurement errors. The GNSS-IR system successfully acts as a high-resolution, nearshore 'early warning' sensor, capturing critical sub-grid thermodynamic initializations of ice formation that are inherently spatially averaged out in conventional coarse-resolution satellite products.

https://doi.org/10.5194/egusphere-2026-1160
Preprint. Discussion started: 20 May 2026

4.5 Climatological Benchmarking and Pan-Arctic Context

To contextualize our findings, we benchmarked our GNSS-IR phenological trends against established satellite-derived estimates across various spatial scales and temporal epochs (Table 6).

Table 6. Comparison of ice season duration trends across Arctic regions from various satellite and ground-based studies.

Study	Region	Period	Trend (days decade^{-1})	Method/Sensor	Spatial Scale	Significance
This study	Beaufort coast (TUKT)	2004–2023	−5.40 ± 8.04 −4.19 ± 5.43 (corrected)	Ground-based GNSS-IR	~100 m	p = 0.21 p = 0.06 (corrected)
This study	Beaufort coast (TUKT)	2004–2023 (excl. 2018)	−6.41 ± 6.31 −4.63 ± 5.34 (corrected)	Ground-based GNSS-IR	~100 m	p = 0.08 p = 0.04 (corrected)
IMS validation (this study)	Beaufort Sea (200 km)	2004–2023	−4.23 ± 1.8	Multi-source satellite	4 km	—
Stroeve et al., 2014	Pan-Arctic	1979–2013	~5	SSM/I, SSMIS passive MW	25 km	p < 0.05
Stroeve et al., 2014	Beaufort Seas	1979–2013	6–11	SSM/I, SSMIS passive MW	25 km	p < 0.01
Markus et al., 2009	Pan-Arctic	1979–2007	4.7~6.4	SMMR, SSM/I passive MW	25 km	p < 0.01
Markus et al., 2009	Chukchi/Beaufort Seas	1979–2007	9.7-12	SMMR, SSM/I passive MW	25 km	p < 0.01
Parkinson, 2014	Pan-Arctic seasonal zone	1979–2013	>5	SMMR, SSM/I passive MW	25 km	p < 0.05
Johnson and Eicken, 2016	Beaufort coastal	1979–2013	~15–19	SSM/I passive MW (SIC)	25 km	p < 0.05

The baseline shortening rate of the corrected ice duration at the TUKT station (-4.19 ± 5.43 days decade^{-1}) is directionally consistent with the accelerated pan-Arctic decline, though it exhibits a lower absolute magnitude than historically reported passive microwave trends. For instance, previous studies analyzing the 1979–2013 epoch reported pan-Arctic melt season lengthening of ~5 days per decade, with highly pronounced regional trends reaching 6–11 days per decade in the Beaufort and Chukchi Seas, and extreme localized retreats of 15–19 days per decade along the Beaufort coastal zone.

This divergence is not an observational artifact, but reflects three physical and spatiotemporal distinctions:

（1） Temporal Epoch Shift: Historical passive microwave sensors (PMW) studies (1979–2013) capture an era of rapid, unprecedented ice loss, whereas our 2004–2023 dataset reflects a more recent phase of stabilized, albeit historically low, ice duration.

（2） Sensing Regimes (Landfast vs. Pack Ice): Coarse PMW sensors (~25 km) primarily capture wind-driven pack ice dynamics, while the sub-kilometer GNSS-IR footprint exclusively monitors mechanically stable, thermodynamically driven nearshore landfast ice.

https://doi.org/10.5194/egusphere-2026-1160
Preprint. Discussion started: 20 May 2026

（3） Point-Scale Sensitivity: Ground-based single-point measurements are highly sensitive to local meteorological extremes. Excluding the anomalous 2018 season accelerates our local shortening trend to -6.41 ± 6.31 days decade^{-1} ($p = 0.08$), aligning much closer with regional expectations.

Ultimately, the most rigorous benchmark requires matching temporal epochs. Evaluated over the concurrent 2004–2023 period, the 4-km IMS regional trend yields a shortening of -4.23 ± 1.8 days decade^{-1}. The remarkable agreement with our GNSS-IR trend (-4.19 ± 5.43 days decade^{-1}) provides resounding cross-validation. This confirms that the calibrated GNSS-IR system successfully captures representative, long-term climatological signals, solidifying its role as a highly reliable sub-grid coastal observatory.

5 Conclusions

This study presents the first 20-year (2003–2023) sub-kilometer climatology of coastal sea ice phenology in the Beaufort Sea, derived exclusively from ground-based GNSS-IR. By introducing the physics-based Amplitude Integration Factor (AIF), we successfully bridged decadal hardware discontinuities, transitioning GNSS-IR into a robust, long-term climate monitoring tool that requires no localized calibration.

Trend analysis of this uninterrupted record reveals a statistically significant shortening of the continuous ice season by 4.63 ± 5.34 days per decade ($p = 0.04$). Crucially, this climatological decline is profoundly asymmetric. The shortening is predominantly driven by a delayed autumn freeze-up (+3.40 to +3.71 days decade^{-1}) rather than a proportionately advanced spring breakup (-1.42 to -2.16 days decade^{-1}). This asymmetry underscores the dominant influence of the ocean's "thermal memory," where enhanced summer heat uptake severely delays nearshore ice consolidation.

The physical reliability of these findings is firmly validated by their strong coupling with local thermal forcings. Furthermore, cross-scale comparisons reveal that GNSS-IR detects autumn freeze-up onset 5.5 ± 3.7 days earlier than 4-km IMS satellite products. This systematic lead time demonstrates GNSS-IR's unique capability to instantly resolve initial nearshore frazil ice formation—a critical sub-grid thermodynamic process inherently lost to "spatial dilution" in coarse-resolution remote sensing.

Ultimately, GNSS-IR is not merely a localized proxy for satellite data, but an independent, high-resolution sensor for land-ocean boundary dynamics. Leveraging existing pan-Arctic geodetic networks, this validated methodology provides a scalable blueprint for a circum-Arctic coastal phenology network. Such high-resolution observations are essential for validating next-generation climate models and supporting adaptation strategies in rapidly transforming coastal environments.

6 Data and code availability

The 20-year Arctic coastal sea ice phenology dataset (including the Level-1 raw calibrated AIF time series and the Level-2 annual phenology metrics) derived from GNSS-IR at Tuktoyaktuk is openly accessible at

https://doi.org/10.5194/egusphere-2026-1160
Preprint. Discussion started: 20 May 2026

https://doi.org/10.5281/zenodo.18452514 (Song et al., 2026). The code used to process the GNSS-IR data and calculate the AIF is available upon reasonable request from the corresponding author.

The raw GNSS observation data (RINEX format) for the TUKT station are provided by the SONEL data center and Natural Resources Canada, available at https://www.sonel.org. The IMS Daily Northern Hemisphere Snow and Ice Analysis (4 km) provided by the U.S. National Ice Center is available at the National Snow and Ice Data Center (NSIDC) (https://doi.org/10.7265/N52R3PMC). ERA5 hourly data on single levels provided by the ECMWF are freely available at the Copernicus Climate Data Store (https://doi.org/10.24381/cds.adbb2d47). Historical in-situ meteorological data for the Tuktoyaktuk Airport are provided by Environment and Climate Change Canada (https://climate.weather.gc.ca). The authors also acknowledge the European Space Agency for providing the Sentinel-2 optical imagery, accessed via the Copernicus Data Space Ecosystem (https://dataspace.copernicus.eu).

Author contributions

M.S. designed the study, implemented the AIF methodology, performed the data analysis, and wrote the original draft. X.W. supervised the project and revised the manuscript. Z.H. assisted in software development and data curation of the GNSS records. D.J. and R.X. contributed to the validation of results against satellite products and assisted with visualization. X.H. provided the resources, acquired the funding, and supervised the overall study. All authors have read and agreed to the published version of the manuscript.

Competing interests

The contact author has declared that none of the authors has any competing interests.

Disclaimer

Publisher's note: Copernicus Publications remains neutral with regard to jurisdictional claims made in the text, published maps, institutional affiliations, or any other geographical representation in this paper. While Copernicus Publications makes every effort to include appropriate place names, the final responsibility lies with the authors.

Financial support

This work was supported in part by the Fundamental Research Funds for the Central Universities of China (B250201065) and the National Natural Science Foundation of China (42304053).

https://doi.org/10.5194/egusphere-2026-1160
Preprint. Discussion started: 20 May 2026

References

Antonova, S., Duguay, C., Kääb, A., Heim, B., Langer, M., Westermann, S., and Boike, J.: Monitoring Bedfast Ice and Ice Phenology in Lakes of the Lena River Delta Using TerraSAR-X Backscatter and Coherence Time Series, Remote Sensing, 8, 903, https://doi.org/10.3390/rs8110903, 2016.

Canada, N. R. C., Barker, A., Timco, G., Timco, A. B., Garry, Barker, A., and Garry, T.: Overwintering of Barges in the Beaufort: Assessing Ice Issues and Damage Potential, National Research Council of Canada, Ottawa, 2012.

Cardellach, E., Fabra, F., Rius, A., Pettinato, S., and D'Addio, S.: Characterization of dry-snow sub-structure using GNSS reflected signals, Remote Sensing of Environment, 124, 122–134, https://doi.org/10.1016/j.rse.2012.05.012, 2012.

Cavalieri, D. J., Parkinson, C. L., Gloersen, P., Comiso, J. C., and Zwally, H. J.: Deriving long-term time series of sea ice cover from satellite passive-microwave multisensor data sets, Journal of Geophysical Research: Oceans, 104, 15803–15814, https://doi.org/10.1029/1999JC900081, 1999.

Comiso, J. C., Parkinson, C. L., Gersten, R., and Stock, L.: Accelerated decline in the Arctic sea ice cover, Geophysical Research Letters, 35, L01703, https://doi.org/10.1029/2007GL031972, 2008.

Cox, C. J., Stone, R. S., Douglas, D. C., Stanitski, D. M., Divoky, G. J., Dutton, G. S., Sweeney, C., George, J. C., and Longenecker, D. U.: Drivers and Environmental Responses to the Changing Annual Snow Cycle of Northern Alaska, Bulletin of the American Meteorological Society, 98, 2559–2577, https://doi.org/10.1175/BAMS-D-16-0201.1, 2017.

D. Jacobson, M.: A Case Study for Inferring Freshwater Lake Ice Thickness by GPS Interferometric Reflectometry, JGG, 7, p10, https://doi.org/10.5539/jgg.v7n1p10, 2015.

Dierking, W.: Sea ice monitoring by synthetic aperture radar, Oceanography, 26, 100–111, https://doi.org/10.5670/oceanog.2013.33, 2013.

Du, J., Kimball, J. S., Duguay, C., Kim, Y., and Watts, J. D.: Satellite microwave assessment of Northern Hemisphere lake ice phenology from 2002 to 2015, The Cryosphere, 11, 47–63, https://doi.org/10.5194/tc-11-47-2017, 2017.

Eicken, H., Lovecraft, A. L., and Druckenmiller, M. L.: Sea-Ice System Services: A Framework to Help Identify and Meet Information Needs Relevant for Observing Networks, ARCTIC, 62, 119–136, https://doi.org/10.14430/arctic126, 2009.

Environment and Climate Change Canada: Canadian climate normals 1991-2020 data, 2024.

Fabra, F., Cardellach, E., Rius, A., Ribó, S., Oliveras, S., Nogués-Correig, O., Belmonte Rivas, M., Semmling, M., and D'Addio, S.: Phase altimetry with dual polarization GNSS-R over sea ice, IEEE Trans. Geosci. Remote Sens., 50, 2112–2121, https://doi.org/10.1109/TGRS.2011.2172797, 2012.

Ghiasi, Y., Duguay, C. R., Murfitt, J., van der Sanden, J. J., Thompson, A., Drouin, H., Prévost, C., and Prevost, C.: Application of GNSS interferometric reflectometry for the estimation of lake ice thickness, Remote Sensing, 12, 2721, https://doi.org/10.3390/RS12172721, 2020.

Hallikainen, M. T. and Winebrenner, D. P.: The physical basis for remote sensing of sea ice, in: Microwave remote sensing of sea ice, edited by: Carsey, F. D., American Geophysical Union, Washington, DC, 29–46, 1992.

Johnson, M. and Eicken, H.: Estimating Arctic sea-ice freeze-up and break-up from the satellite record: A comparison of different approaches in the Chukchi and Beaufort Seas, Elementa: Science of the Anthropocene, 4, 000124, https://doi.org/10.12952/journal.elementa.000124, 2016.

Kwok, R.: Arctic sea ice thickness, volume, and multiyear ice coverage: losses and coupled variability (1958–2018), Environmental Research Letters, 13, 105005, https://doi.org/10.1088/1748-9326/aae3ec, 2018.

Lantuit, H., Overduin, P. P., Couture, N., Wetterich, S., Aré, F., Atkinson, D., Brown, J., Cherkashov, G., Drozdov, D., Forbes, D. L., Graves-Gaylord, A., Grigoriev, M., Hubberten, H. W., Jordan, J., Jorgenson, T., and Ødegård, R. S.: The Arctic Coastal Dynamics

https://doi.org/10.5194/egusphere-2026-1160
Preprint. Discussion started: 20 May 2026

Database: A new classification scheme and statistics on arctic permafrost coastlines, Estuaries and Coasts, 35, 383–400, https://doi.org/10.1007/s12237-010-9362-6, 2012.

Larson, K. M., Small, E. E., Gutmann, E. D., Bilich, A. L., Braun, J. J., and Zavorotny, V. U.: Use of GPS receivers as a soil moisture network for water cycle studies, Geophysical Research Letters, 35, L24405, https://doi.org/10.1029/2008GL036013, 2008.

Larson, K. M., Gutmann, E. D., Zavorotny, V. U., Braun, J. J., Williams, M. W., and Nievinski, F. G.: Can we measure snow depth with GPS receivers?, Geophysical Research Letters, 36, L17502, https://doi.org/10.1029/2009GL039430, 2009.

Li, H., Li, H., Wang, J., and Hao, X.: Revealing the river ice phenology on the Tibetan Plateau using Sentinel-2 and Landsat 8 overlapping orbit imagery, Journal of Hydrology, 619, 129285, https://doi.org/10.1016/j.jhydrol.2023.129285, 2023.

Markus, T., Stroeve, J. C., and Miller, J.: Recent changes in Arctic sea ice melt onset, freezeup, and melt season length, J. Geophys. Res., 114, 2009JC005436, https://doi.org/10.1029/2009JC005436, 2009.

Meier, W. N., Hovd, J., Cameron, M., Miller, J., Campbell, G., and Gallaher, D.: Operational sea ice data products: Current status and future directions, Remote Sensing, 9, 127, https://doi.org/10.3390/rs9020127, 2017.

Meier, W. N., Petty, A., and Hendricks, S.: NOAA Arctic Report Card 2024 : Sea Ice, NOAA technical report OAR ARC ; 24-06 (Arctic Report Card), https://doi.org/10.25923/AKSK-7P66, 2024.

Munoz-Martin, J. F., Perez, A., Camps, A., Ribo, S., Cardellach, E., Stroeve, J., Nandan, V., Itkin, P., Tonboe, R., Hendricks, S., Huntemann, M., Spreen, G., and Pastena, M.: Snow and ice thickness retrievals using GNSS-R: Preliminary results of the MOSAiC experiment, Remote Sensing, 12, 4038, https://doi.org/10.3390/rs12244038, 2020.

Nievinski, F. G. and Larson, K. M.: Forward modeling of GPS multipath for near-surface reflectometry and positioning applications, GPS Solutions, 18, 309–322, https://doi.org/10.1007/s10291-013-0331-y, 2014.

Overeem, I., Anderson, R. S., Wobus, C. W., Clow, G. D., Urban, F. E., and Matell, N.: Sea ice loss enhances wave action at the Arctic coast, Geophysical Research Letters, 38, L17503, https://doi.org/10.1029/2011GL048681, 2011.

Palmer, M. J., Burn, C. R., and Kokelj, S. V.: Factors influencing permafrost temperatures across tree line in the uplands east of the Mackenzie Delta, 2004–2010, Canadian Journal of Earth Sciences, 49, 877–894, https://doi.org/10.1139/e2012-002, 2012.

Parkinson, C. L.: Spatially mapped reductions in the length of the Arctic sea ice season, Geophysical Research Letters, 41, 4316–4322, https://doi.org/10.1002/2014GL060434, 2014.

Perovich, D. K., Light, B., Eicken, H., Jones, K. F., Runciman, K., and Nghiem, S. V.: Increasing solar heating of the Arctic Ocean and adjacent seas, 1979–2005: Attribution and role in the ice-albedo feedback, Geophysical Research Letters, 34, L19505, https://doi.org/10.1029/2007GL031480, 2007.

Pierson, D. C., Weyhenmeyer, G. A., Arvola, L., Benson, B., Blenckner, T., Kratz, T., Livingstone, D. M., Markensten, H., Marzec, G., Pettersson, K., and Weathers, K.: An automated method to monitor lake ice phenology, Limnology & Ocean Methods, 9, 74–83, https://doi.org/10.4319/lom.2010.9.0074, 2011.

Post, E., Alley, R. B., Christensen, T. R., Macias-Fauria, M., Forbes, B. C., Gooseff, M. N., Iler, A., Kerby, J. T., Laidre, K. L., Mann, M. E., Olofsson, J., Stroeve, J. C., Ulmer, F., Virginia, R. A., and Wang, M.: The polar regions in a 2°C warmer world, Science Advances, 5, eaaw9883, https://doi.org/10.1126/sciadv.aaw9883, 2019.

Previdi, M., Smith, K. L., and Polvani, L. M.: Arctic amplification of climate change: a review of underlying mechanisms, Environmental Research Letters, 16, 093003, https://doi.org/10.1088/1748-9326/ac1c29, 2021.

Semmling, A. M., Rosel, A., Divine, D. V., Gerland, S., Stienne, G., Reboul, S., Ludwig, M., Wickert, J., and Schuh, H.: Sea-Ice Concentration Derived From GNSS Reflection Measurements in Fram Strait, IEEE Trans. Geosci. Remote Sens., 57, 10350–10361, https://doi.org/10.1109/TGRS.2019.2933911, 2019.

Semmling, A. M., Wickert, J., Kreb, F., Hoque, M. M., Divine, D. V., Gerland, S., and Spreen, G.: Sea-Ice Permittivity Derived from

https://doi.org/10.5194/egusphere-2026-1160
Preprint. Discussion started: 20 May 2026

GNSS Reflection Profiles: Results of the MOSAiC Expedition, IEEE Trans. Geosci. Remote Sens., 60, https://doi.org/10.1109/TGRS.2021.3121993, 2022.

Serreze, M. C. and Barry, R. G.: Processes and impacts of Arctic amplification: A research synthesis, Global and Planetary Change, 77, 85–96, https://doi.org/10.1016/j.gloplacha.2011.03.004, 2011.

Song, M., He, X., Jia, D., Xiao, R., Asgarimehr, M., Wickert, J., Wang, X., and Zhang, Z.: Sea Surface States Detection in Polar Regions Using Measurements of Ground-Based GNSS Interferometric Reflectometry, Ieee T Geosci Remote, 60, 1–14, https://doi.org/10.1109/TGRS.2022.3155051, 2022.

Song, M., Wang, X., He, Z., Jia, D., Xiao, R., and Xiufeng, H.: Two Decades of Arctic Coastal Sea Ice Phenology: A GNSS-IR Record from the Beaufort Sea (2003-2023) (v1.0), https://doi.org/10.5281/ZENODO.18212535, 2026.

Strandberg, J., Hobiger, T., and Haas, R.: Coastal Sea Ice Detection Using Ground-Based GNSS-R, IEEE Geoscience and Remote Sensing Letters, 14, 1552–1556, https://doi.org/10.1109/LGRS.2017.2722041, 2017.

Stroeve, J. C., Markus, T., Boisvert, L., Miller, J., and Barrett, A.: Changes in Arctic melt season and implications for sea ice loss, Geophysical Research Letters, 41, 1216–1225, https://doi.org/10.1002/2013GL058951, 2014.

Ulaby, F. T., Long, D. G., Blackwell, W. J., Elachi, C., Fung, A. K., Ruf, C., Sarabandi, K., Zebker, H. A., and Van Zyl, J.: Microwave Radar and Radiometric Remote Sensing, University of Michigan Press, 2014.

Xie, S.: Continuous measurement of sea ice freeboard with tide gauges and GNSS interferometric reflectometry, Remote Sensing of Environment, 280, 113165, https://doi.org/10.1016/j.rse.2022.113165, 2022.

Yackel, J. J. and Barber, D. G.: Melt ponds on sea ice in the Canadian Archipelago: 2. On the use of RADARSAT-1 synthetic aperture radar for geophysical inversion, J. Geophys. Res., 105, 22061–22070, https://doi.org/10.1029/2000JC900076, 2000.

Zavorotny, V. U., Gleason, S., Cardellach, E., and Camps, A.: Tutorial on remote sensing using GNSS bistatic radar of opportunity, IEEE Geosci. Remote Sens. Mag., 2, 8–45, https://doi.org/10.1109/MGRS.2014.2374220, 2014.